


Noninvasive measurement of local temperature using ultrasound-switchable fluorescence

LIQIN REN,^{1,2}  TINGFENG YAO,^{1,2} KYTAI T. NGUYEN,^{2,3} AND BAOHONG YUAN^{1,2,*}

¹Ultrasound and Optical Imaging Laboratory, Department of Bioengineering, The University of Texas at Arlington, Arlington, TX 76019, USA

²Joint Biomedical Engineering Program, The University of Texas at Arlington and The University of Texas Southwestern Medical Center at Dallas, Dallas, TX 75390, USA

³Department of Bioengineering, The University of Texas at Arlington, Arlington, TX 76019, USA

*baohong@uta.edu

Abstract: Measuring the local background temperature in diseased and inflamed tissues is highly desirable, especially in a non-invasive way. In this work, ultrasound-switchable fluorescence (USF) technique was utilized to estimate the local background temperature for the first time by analyzing the temperature dependence of fluorescence emission from USF contrast agents induced by a focused ultrasound (FU) beam. First, temperature-sensitive USF agents with distinct temperature switching-on thresholds were synthesized, and their thermal switching characteristics were quantified using an independent spectrometer system. Second, the USF contrast agent suspension was injected into a microtube that was embedded into a phantom and the dynamic USF signal was acquired using a camera-based USF system. The differential profile of the measured dynamic USF signal was computed and compared with the thermal switching characteristics. This allowed for the calculation of the local background temperature of the sample in the FU focal volume based on the estimation of heating speed. An infrared (IR) camera was used to acquire the surface temperature of the sample and further compare it with the USF system. The results showed that the difference between the temperatures acquired from the USF thermometry and the IR thermography was 0.64 ± 0.43 °C when operating at the physiological temperature range from 35.27 to 39.31 °C. These results indicated the potential use of the USF system for measuring the local temperature in diseased tissues non-invasively. The designed USF-based thermometry shows a broad application prospect in high spatial resolution temperature imaging with a tunable measurement range in deep tissue.

© 2023 Optica Publishing Group under the terms of the [Optica Open Access Publishing Agreement](#)

1. Introduction

Tissue temperature is largely dependent on cell metabolism and local blood flow. For example, most solid tumors generate more heat than surrounding healthy tissues due to increased vascularization and metabolic activity [1]. It has been examined that the temperature of lung, bladder, and breast tumors often had a 1-2 °C higher temperature than the surrounding healthy tissues [2–5]. In cancerous breast tissue, there are two main changes in temperature: (1) an elevated absolute temperature in the tumor area, and (2) a distorted spatial distribution of temperature, with oscillations around the tumor boundary [6].

These results stimulated researchers to consider temperature as an indicator of tumor physiological activeness for screening and/or diagnosis purposes. It directly led to the prevalence of breast thermography for breast cancer screening in the 1960s -1980s [6–10]. However, thermography failed in the competition with x-ray-based mammography eventually [11]. The issue with thermography lies in its reliance on infrared photon detection within a wavelength spectrum of approximately 3-10 microns for imaging temperature. In cases where these infrared photons generated from deep breast tissues are completely absorbed by water molecules present

in the tissue, leading to a complete loss of information beneath the skin. Unfortunately, the absolute value of the surface temperature is not specific to the tumor's activeness and can be affected by many other factors [12,13]. Thus, breast thermography diagnosis based on skin surface temperature is neither specific nor sensitive to tumor activeness for diagnosis purposes.

In contrast, x-ray-based mammography can visualize tissue well beyond the skin and provide clear anatomic or structural information of tumors, which were much more specific and sensitive than thermography. However, over the years since the adoption of mammography for breast cancer screening, many shortcomings have been realized, such as possible overdiagnosis, using ionizing radiation, uncomfortable patient experience due to significant compression of patient's breasts, low specificity (especially for small lesions and women with dense breasts), and lack of physiological or functional information [14–16].

Based on the discussion above, we speculated that the measurement of local tumor temperature and its gradient, beneath the surface of the breast, could serve as a valuable tool for assessing tumor activeness and offering risk stratification. This could potentially identify subsets of women, particularly those with small lesions or dense breast tissue, which may reduce the need for biopsy and mitigate overdiagnosis. Unfortunately, even today this indicator still cannot be fully adopted due to several challenges of current technologies: (1) limited temperature sensitivity and (2) difficulty to measure the absolute local tissue temperature. Temperature sensitivity can be quantified by the percent of signal change when temperature increases by one degree (°C). In magnetic resonance imaging (MRI)-based thermometry, temperature sensitivity is < 2% per °C in the spin-lattice relaxation method, which leads to a limited temperature resolution of ~1 °C in a clinical scanner and ~0.3-0.5 °C in a pre-clinical scanner with a strong magnetic field [17–19]. Ultrasound-based thermometry has even lower temperature sensitivity (~0.05% per °C) and temperature resolution [20,21]. Photoacoustic-based thermometry has relatively higher sensitivity (~4-5% per °C), but this sensitivity is still very limited [21–35]. In addition, most technologies aim to image the relative change in tissue temperature induced by externally applied energy (such as high intensity focused ultrasound or other radiation), including MRI-, ultrasound-, and photoacoustic-based thermometry, but imaging local background temperature in tissues is much less investigated [35].

To overcome these limitations in thermography, thermometry, and mammography, we investigated a new, sensitive, and robust method based on our ultrasound-switchable fluorescence (USF) technology [36–40]. Indocyanine green (ICG), an FDA-approved near-infrared (NIR) fluorophore, was encapsulated into nanometer-sized liposomes (ICG-liposomes), which showed excellent temperature sensitivity and has been demonstrated as an excellent USF imaging agent [41,42]. A unique feature of this type of USF agent is that the fluorescence intensity can increase ~2-3 times when temperature rises ~2-3 °C. Thus, it leads to an 'OFF-ON' switch in fluorescence in a narrow range of the temperature rise, and further provides a significantly high temperature sensitivity, > 100% per °C [41,42]. More importantly, this method enables the direct quantification of tissue's absolute temperature. These features make it an ideal technology to map tumor subtle temperature variations. In this study, a blood vessel-mimic phantom was adopted. The USF-based thermometry shows good agreement with IR thermal imaging and the average difference is 0.64 ± 0.43 °C. The success of this study provides evidence for the feasibility of USF-based thermometry as a potentially viable technique for non-invasive measurement of local tissue temperature.

2. Operation principles experimental setup

2.1. Principle of background temperature measurement

Liposome-based USF contrast agents typically exhibited a sharp fluorescence transition from an off to an on state when the environmental temperature rises above a threshold, the lower critical solution temperature (LCST) [41,42]. Thus, their fluorescence-vs-temperature profiles appeared

sharp step functions. In USF imaging, to avoid liposomes being switched on by surrounding tissue, the LCST was usually controlled slightly above the background tissue temperature. To externally switch on the fluorophores, an ultrasound pulse was usually applied to increase the tissue temperature in its focal volume above the LCST. These ultrasound-induced fluorescence photons were called USF signal. In addition, the threshold (i.e., the LCST) could be easily controlled by adjusting the lipids compositions of the outer liposomal shell. Based on these studies, we speculated that if we could synthesize two liposomes with distinct LCSTs and mix them we might be able to estimate the ultrasound heating speed and further the background temperature based on the USF signal. We can control the second threshold ($LCST_2$) higher than the first one ($LCST_1$) but both LCSTs are higher than tissue background temperature (T_t). When the ultrasound pulse is applied, the temperature in the focal volume increases from the background temperature, passing the $LCST_1$, and eventually to somewhere above $LCST_2$. When the temperature rises somewhere above $LCST_1$ but below $LCST_2$ (denoted as T_a) at time t_a , we expect to observe the first quickest increase in the USF signal, which is mainly generated from the first liposome. This indicates that the temperature in the focal volume reaches the value (T_a) that corresponds to the highest slope of the step function of the fluorescence-vs-temperature profile curve of the first liposome.

When the temperature further increases above the $LCST_2$, the second liposomes will be switched on, leading to a further increase in USF signal. Similarly, when the temperature reaches somewhere above the $LCST_2$ (denoted as T_b) at time t_b , we expect to observe the second quickest increase in the USF signal, which is primarily generated from the second liposome. T_b is the temperature where the highest slope of the fluorescence-vs-temperature profile curve of the second liposome is reached.

By analyzing these speed changes in the USF signal, we can identify the specific time points (t_a and t_b). Based on the assumption that the tissue temperature in the ultrasound focal volume reaches T_a at t_a and T_b at t_b , a linear heating speed can be calculated as $V_h = (T_b - T_a) / (t_b - t_a)$. If the thermal diffusion can be ignored during the heating due to the short ultrasound exposure, the tissue background temperature (T_t) can be calculated as $T_t = T_a - V_h * (t_a - t_0) = T_b - V_h * (t_b - t_0)$, where t_0 is the time when the ultrasound pulse is initiated and usually can be set as zero if the system is synchronized by the trigger. In practice, T_t can also be equivalently calculated via a linear fitting based on the temperature-vs-time points (i.e., $[T_a, T_b]$ vs $[t_a, t_b]$) by extracting the intercept on the temperature axis, which indicates the background temperature right before the ultrasound exposure (i.e., $[T_t, t_0 = 0]$). Note that T_a and T_b (and LCSTs) can be independently found by measuring the characteristic curves of the fluorescence-vs-temperature profiles of the two liposomes and their mixture, and the two time points (t_a and t_b) can be found based on the rate of change of the dynamic USF signal.

2.2. Materials

Ethanol and cholesterol were from Fisher Scientific International, Inc., USA. ICG was obtained from Chem-Impex Int'l Inc., USA. 1, 2-dipalmitoyl-sn-glycero-3-phosphocholine (DPPC) and 1,2-distearoyl-sn-glycero-3-phosphocholine (DSPC) were purchased from Avanti Polar Lipids, Inc., USA.

2.3. Liposome preparation

The liposomes were prepared via ethanol injection method [43]. 20 mg phospholipids (DPPC and DSPC) and 1 mg cholesterol were dissolved in 700 μ L ethanol. The resultant organic phase was injected into 9 mL of ICG aqueous phase (0.06 mg/mL) under magnetic stirring at 1000 rpm. After stirring for 15 mins, the residual ethanol was removed by rotary evaporation under reduced pressure. The liposome suspension was then purified by ultracentrifugation (Avanti J-E, Beckman Coulter, USA) at 16,500 rpm for 25 min. In this study, the mass ratio of DPPC and DSPC is 1.5

for the first liposome (denoted by L) with a lower threshold $LCST_1$, while the lipids ratio is 0.6 for the second liposome (denoted by H) with a higher threshold $LCST_2$. The liposomal mixture was prepared with a volume ratio of L:H = 1:4.

2.4. Characterizations methods

The hydrodynamic size and polydispersity index of the liposomal samples were obtained by a dynamic light scattering instrument (NanoBrook 90PlusPALS, Brookhaven Instruments, USA). All measurements were performed in triplicate at room temperature.

An in-house built spectrometer system was used to measure the fluorescence intensity with respect to temperature [44]. The fluorescent sample in a 3 mL quartz cuvette was placed into a temperature-controlled holder (Quantum Northwest, Inc., USA) and excited by an 808 nm laser (MGL-II-808-2W, Dragon Lasers, China). A modular USB spectrometer (USB2000+, Ocean Inlight, USA) was used to acquire the spectra, and the fluorescence level was a sum of emission spectra beyond 830 nm.

2.5. Camera-based USF system

The experiments were carried out in the electron multiplying charge-coupled device (EMCCD) camera-based USF system [45,46]. Figure 1(a) shows the schematic diagram of the in vitro study of the thermometry system. Briefly, a silicone tube (Inner diameter = 0.30 mm; Outer diameter = 0.64 mm) embedded in the silicone phantom with a thickness of 4 mm was filled with thermosensitive agents and illuminated by the light beam from an 808 nm laser (MGL-II-808-2W, Dragon Lasers, China). The fluorescence passed through three long-pass filters (BLP01-830R-50/25, Semrock Inc., USA), and then was captured by an EMCCD camera (ProEM-HS: 1024BX3, Princeton Instruments, USA) with a camera lens (AF NIKKOR 50 mm f/1.8D Lens, Nikon, Japan). A function generator (FG, 33500B, Agilent, USA) generated the driven voltage to a 2.5 MHz FU transducer (H-108, Sonic Concepts Inc., USA) after being amplified by a 50 dB-gain radio frequency power amplifier (RF-AMP, A075, E&I, USA) and then passing through the matching network (MNW). To provide independent validation of the temperature values, an IR camera (A300, Teledyne FLIR, USA) was also synchronized by receiving trigger signals from a pulse delay generator (PDG, P40, Highland Technology, USA) connected to the FG. The temperature of the water was controlled by a temperature controller system (PTC10, Stanford Research Systems, USA). The temperature probe submerged in the water was placed near the tube to get a close estimation of the temperature of the USF agents. A magnetic stirrer with a magnetic bar (11-100-16S, Fisher Scientific, USA) was used to ensure a relatively uniform temperature distribution in the water tank.

The purposes of using a relatively thin silicone sample in this feasibility study are mainly due to two reasons: (1) Combining the small thickness with the transparency of silicone to IR light, the IR-camera-measured temperature from the sample surface should be approximately equal to the temperature in the sample; (2) To enable the acquisition of dynamic signals at a high frame rate using the EMCCD camera, a strong USF signal without significant attenuation is required.

Figure 1(b) explains the time sequences and synchronization between USF imaging system and IR thermal camera. For all experiments, the heating FU pulse with a duration of 1.2 s was triggered 0.1 s after the EMCCD camera started acquiring. EMCCD camera was initiated by the trigger command sent by the computer (Trigger 1), while the FU transducer was externally triggered by the function generator. Both the function generator and EMCCD were synchronized by executing the customized MATLAB script on the computer. The frame rate of the EMCCD camera was 100 Hz. The IR reading was performed synchronously with the camera acquisition after FU exposure, and a single IR thermograph was obtained right before the FU heating to evaluate the background temperature at the target zone. The 10 frames obtained from the EMCCD camera before the FU exposure were averaged and considered as the background fluorescence

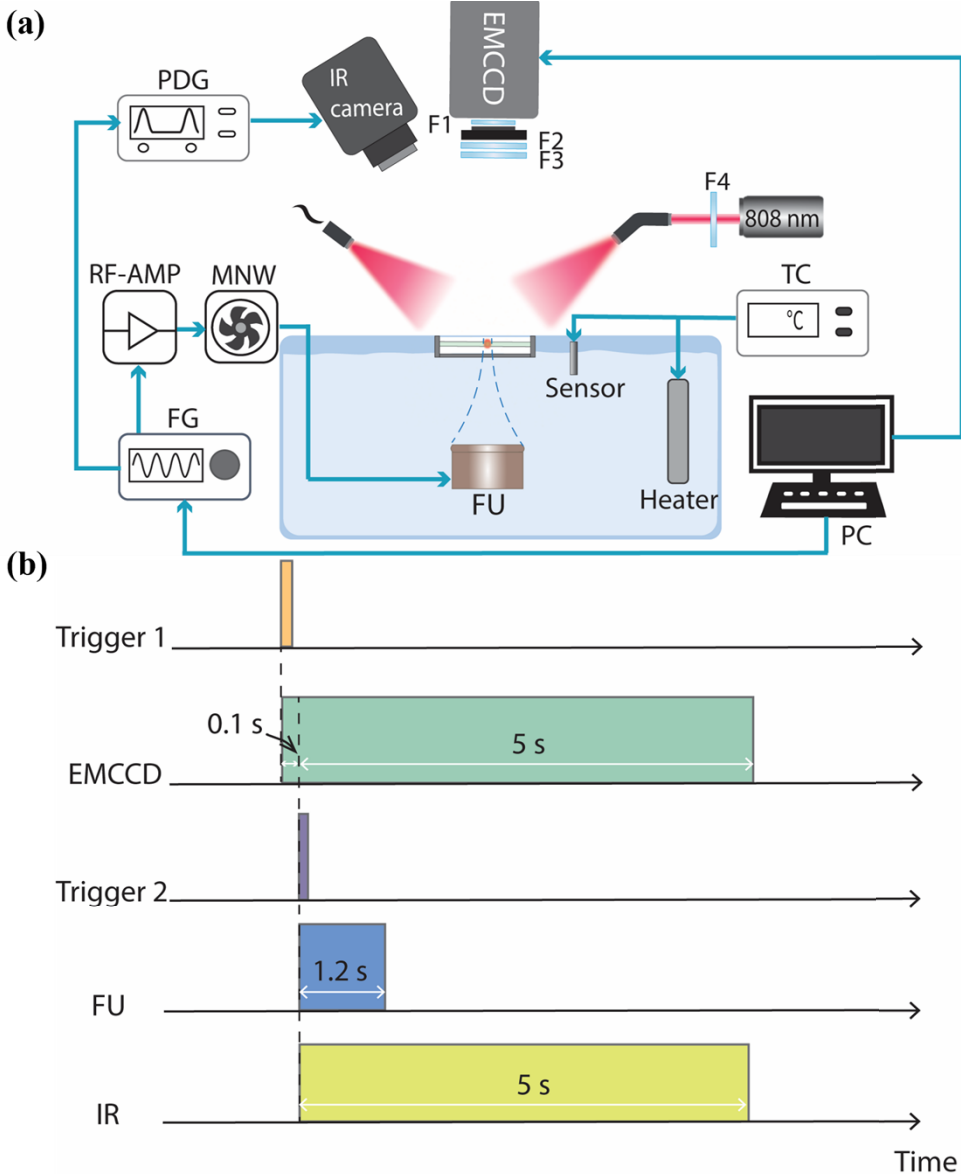


Fig. 1. (a) Schematic diagram of the USF thermometry. PDG: pulse delay generator; RF-Amp: radio-frequency power amplifier; MNW: matching network; FU: focused ultrasound; FG: function generator; F1-3: emission filters (830 Long-pass); F4: excitation filter (785/62 Band-pass); TC: temperature controller. (b) Time sequence diagram of each temperature measurement.

image. The time point when the FU initiated and the rising edge of Trigger 2 occurred can be denoted as t_0 . A continuous set of 500 fluorescence frames was captured immediately (at t_0) to monitor the real-time change of fluorescence in the focal area.

2.6. Fluorescence signal processing

This section explains the procedures for acquiring and processing the signals and further estimating the local temperature based on the acquired dynamic USF signal. The main procedures include measuring the fluorescence-vs-temperature based on two characteristic profiles of the two liposomes and their mixture in cuvettes, and the dynamic USF signals in tissue phantoms from the mixture of the two liposomes. After these profiles are acquired, their differential profiles (i.e., the first-order derivative profiles) are calculated by subtracting any two adjacent data points. The local peaks of these differential profiles are found and used as the characteristic parameters for background temperature estimation via the principle mentioned above (See Section 2.1).

First, the fluorescence emission signals from each of the two liposome samples and their mixture were measured as a function of temperature in a range from 34 to 54 °C with a step size of 0.1 °C using the in-house built spectrometer system. Thus, three switching curves were acquired and the first-order derivatives of each curve were calculated. A total of four local peaks were found from the differential profiles (one from each sample and two from the mixed sample). The dynamic USF signal of the mixed contrast agents was acquired from our camera-based USF system. Briefly, a continuous series of fluorescence images were acquired before, during, and after the FU exposure. The images acquired before the exposure were subtracted from those acquired during and after the exposure. The subtracted images represented the USF signals at different time points. These subtracted images were subsequently and spatially filtered based on the correlation between a normalized averaging filter. Then, the USF intensity values of each USF image were averaged within a $0.33 \times 0.66 \text{ mm}^2$ region of interest from the center of the heating spot, where the temperature distribution was relatively uniform. The computation of the temporal variation of USF intensity can be achieved following the steps mentioned above.

The differential profile of the dynamic USF signal from the mixed liposomes was computed similarly by subtracting any two adjacent data points of the USF signal, and then normalized. Two switching peaks can be found in the time domain, corresponding to two fast-switching temperatures revealed by the characteristic curves of the sample curves measured from the cuvettes. As a result, the information in both time and temperature domains corresponding to each switching peak can be found. As mentioned above, if the thermal diffusion in the focal volume can be ignored within such a short FU exposure, the local background temperature of the sample can be calculated based on the methods discussed previously in Section 2.1.

3. Results and discussion

3.1. Characterizations of fluorescence-vs-temperature profiles of the ICG-Liposomes in cuvettes

Figure 2(a) shows the temperature-dependent fluorescence profiles of the liposomes and their differential profiles. The red dashed line with circles for the liposomes with a high LCST (43.8 °C) and the green dashed line with triangles shows the profiles of the liposomes with a low LCST (38.9 °C). Their differential profiles are represented by the corresponding solid lines, respectively.

Clearly, the fluorescence-vs-temperature profiles exhibit a step function, which is a typical feature required in USF imaging [36,41]. This fact indicates that the ICG-liposomes can be thermally switched on at different LCSTs over sharp transition bands. In addition, each differential profile shows a peak, representing the highest speed of the fluorescence rising at a specific temperature.

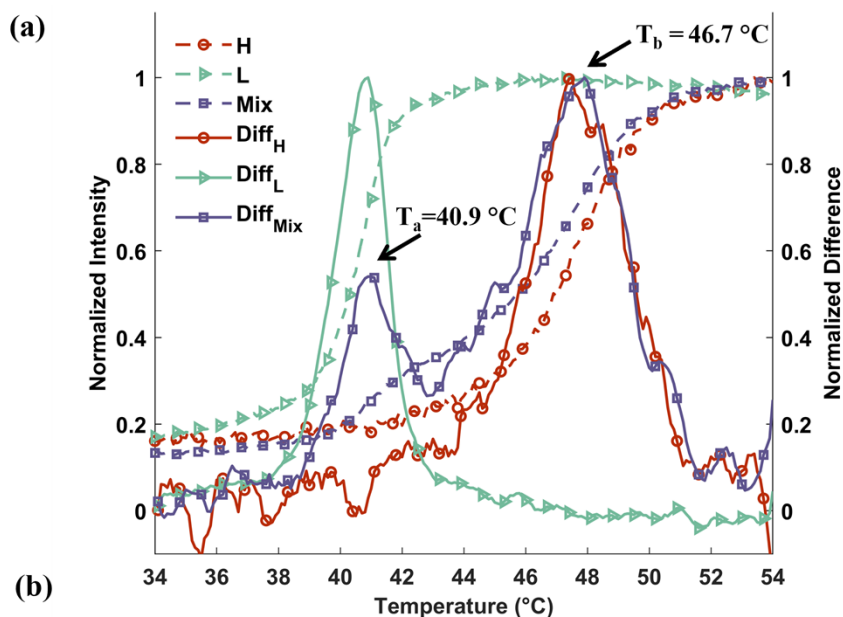


Fig. 2. (a) The normalized fluorescence intensity (solid lines) and the corresponding differences (dashed lines) as a function of temperature when testing the ICG-liposomes in the cuvette using a spectrometer. H: ICG-liposomes with a higher LCST; L: ICG-liposomes with a lower LCST; Mix: The mixtures of H and L with volume ratio of 4:1. Diff: the differences of fluorescence intensity of two adjacent points calculated from the corresponding solid line. (b) The characteristics of ICG-liposomes (H and L).

The ICG-liposomes had similar sizes, polydispersity index (PDI), and zeta potential as illustrated in Fig. 2(b). All liposomes had PDI values below 0.31, demonstrating the homogeneity of liposomes. ICG-liposomes with the high LCST (43.8 °C) are labeled with H and have an average size of 368.86 ± 14.37 nm with narrow size distribution ($PDI = 0.27 \pm 0.09$) and neutral zeta potential at -0.76 ± 0.61 mV. The ICG-liposome with the low LCST (38.9 °C) is denoted as L and has a size of 414.94 ± 62.85 nm with narrow size distribution ($PDI = 0.31 \pm 0.07$) and neutral zeta potential at -0.27 ± 0.94 mV. The low LCST liposome shows a relatively narrower transition band (3.1 °C) relative to the high LCST liposomes (6.8 °C). The LCST shift from high (43.8 °C) to low (38.9 °C) is mainly caused by the increase in the mass ratio between the two main components of DPPC and DSPC from 0.6 to 1.5. The primary components of the liposomal shell are DSPC and DPPC, each possessing a distinct phase transition temperature of 55 °C and 41 °C, respectively [47]. Therefore, LCSTs of liposomal USF agents can be tuned effectively by varying the DPPC: DSPC ratio.

The fluorescence-vs-temperature profile of the mixed liposomes (with a volume ratio of H:L = 4:1) and its differential profile are also plotted in Fig. 2(a) as the dashed purple line with squares and the solid purple line with squares, respectively. The switching property is preserved although the shape is changed compared with that of its individual component. Two peaks can be found from the differential profiles (40.9 and 46.7 °C), representing two local maximum speeds of the fluorescence rising and being related to the peaks of the individual components. These

two temperature values (40.9 and 46.7 °C) will be used as T_a and T_b , respectively, and will be mapped to the USF dynamical signal for calculating background temperature.

3.2. Dynamic USF signal and its derivative of the mixed liposomes in a tissue phantom

As illustrated in Fig. 3(a), the dynamic USF signal and its derivative are displayed by the red dashed line with circles and the solid light green line, respectively. An inset of USF signals over 5 s is also shown in Fig. 3(a), and the USF signal was gradually decreasing after the FU exposure. The background temperature of the USF agents in Fig. 3(a) was 36.85 °C, which was below the first temperature peak ($T_a = 40.9$ °C) as characterized in Fig. 2(a). The voltage from the function generator was 56 mV, which was amplified 50 dB by the power amplifier (RF-AMP) before being applied to the ultrasound transducer. The transmitted electrical power was estimated to be 0.39 W. The lateral and axial sizes of acoustic intensity focus were 0.55 and 2.8 mm, respectively [48]. The comparison between the 2D distribution of temperature in the focal zone acquired by IR camera and 2D distribution of USF collected by EMCCD is provided in Fig. S1.

To demonstrate the USF raw data, five 2D fluorescence images acquired at the time points from $t_1 = 0.10$ s to $t_5 = 1.00$ s by the EMCCD camera during the procedure are also displayed in Fig. 3(b). The USF signal increases over time immediately after the starting of the FU exposure at $t_0 = 0$ s and reaches the maximum when the FU exposure stops at 1.2 s. Similar results can also be seen from the 2D fluorescence images. Also, the first and second peaks of the differential curve of the USF signal appear at $t_2 = 0.18$ s and $t_3 = 0.47$ s, which correspond to the t_a and t_b as discussed before. Obviously, the USF signal does not show a linear relationship with time. This can be seen from its differential curve, which is not a constant. In the early period of the FU exposure (such as $t < t_3 = 0.47$ s), the speed of USF signal remains in a rising period. After that, the speed falls gradually. This non-linear relationship is caused by two factors. First, in the rising period from 0 to t_3 , the thermal energy is usually confined in the focal volume (i.e., so-called thermal confinement) so that thermal diffusion can be ignored, and the temperature grows linearly within the FU exposure time (i.e. the heating speed usually remains a constant in this period). Thus, the non-linearity of the USF signal is mainly caused by the nonlinear features of the step function of the fluorescence-vs-temperature of the two liposomes, rather than the heating. In the late period (such as after t_3), the thermal diffusion may not be ignorable. Thus, the non-linearity of the USF signal is caused by both the nonlinear thermal response of the liposomes and the thermal diffusion. Therefore, restricting t_a and t_b to the early rising period of USF signal or remaining a short ultrasound exposure is necessary to satisfy the thermal requirement and enable the assumption of a constant ultrasound heating speed in this study. In the situation when thermal confinement is not satisfied, more accurate models should be adopted for the background temperature estimation, which will be studied in the future.

3.3. Temperature estimation and precision

Figure 4(a) displays the estimated background temperature (T_t) from our USF method vs. the one measured from the IR camera. The background temperature of the liposome mixture was controlled and varied from 35.27 to 39.31 °C based on the IR camera reading. A solid line is also plotted as a reference to indicate the ideal situation. In general, the USF-estimated background temperature data points should be closely aligned with the reference line, indicating a high degree of correlation between the variables being compared (IR readings in this case). Quantitatively, based on all these data points in Fig. 4(a), the average temperature difference between the two methods was 0.64 ± 0.43 °C. In this study, we limited our measurements to a small range (from 35.27 to 39.31 °C) to match the typical physiological temperature. The measurement range can be modulated by the composition of the lipid shells. For instance, DSPC, DPPC, and dimyristoyl phosphatidylcholine (DMPC) are fully saturated lipids with different lengths of hydrocarbon chains. DMPC exhibits a phase transition temperature that is below body temperature at 24 °C,

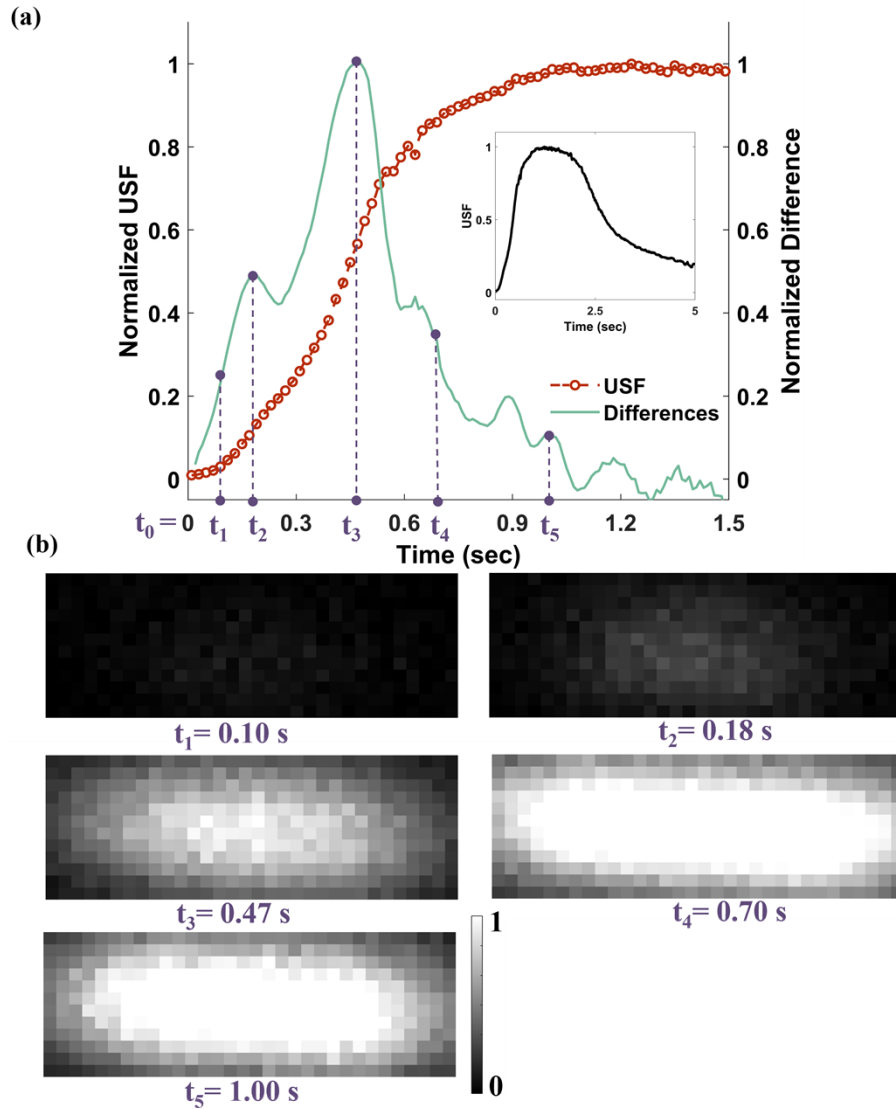


Fig. 3. (a) A demonstration of temporal USF curve (red line) and the calculated differential curve (green line) obtained from the camera-based USF system. Inset: USF signals over 5 s. (b) The acquired USF signals with background subtracted ($0.33 \times 0.99 \text{ mm}^2$ view) at various time points (t_{1-5}).

while the other two phospholipids can transit around and above the physiological temperatures [49].

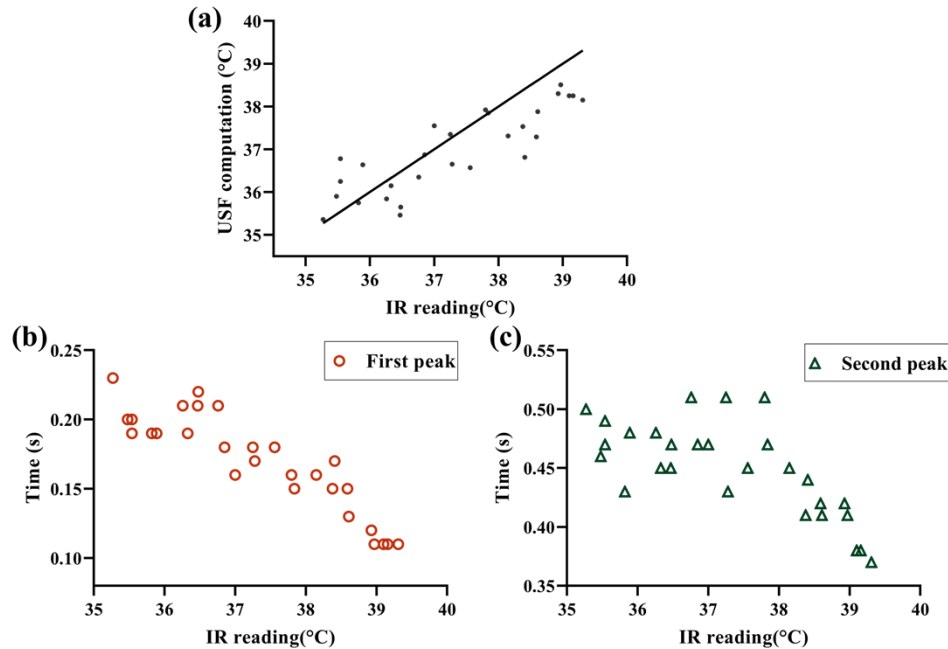


Fig. 4. (a) The temperature estimated by USF thermometry versus IR camera. A reference line with a slope of 1 is added to show the agreements between IR reading and the results from USF thermometry. (b) The occurrence time of the first fast-switching peak at various background temperatures. (c) The time at which the second switching peak occurs at different background temperatures.

Figures 4(b)-(c) display how the two peak times (t_a and t_b) shift with the increase of the background temperature. When the background temperature increases, both t_a and t_b decrease, which means the two peaks occur earlier. These results are understandable based on the discussion below. Because T_a and T_b of the liposomes are mainly dependent upon the properties of the material component of the liposomes, it is reasonable to assume they are stable during our experiments. Increasing the background temperature (T_1) will lead to the reduction of the temperature difference between the background temperature and the T_a (and also T_b). In this experiment, the FU heating speed is considered to be fixed. Thus, the required duration for raising the temperature of the sample from T_1 to T_a or T_b decreases. On the other hand, if subtracting the data in Fig. 4(b) from the data in Fig. 4(c), one can obtain the time difference, $t_b - t_a$, which represents the time that is needed for heating the sample from T_b to T_a . The results show that this difference remained relatively constant at approximately 0.28 ± 0.03 s. This further indicates that the FU heating speed roughly remained a constant (i.e., $V_h = (T_b - T_a)/(t_b - t_a) = (46.7 - 40.9)^\circ\text{C}/0.28 \text{ s} \approx 20.71^\circ\text{C/s}$) during this experiment.

3.4. Effects of other experimental parameters

Figure 5(a) shows one example of how the ultrasound strength (therefore the heating speed) affects t_a and t_b when the background temperature was kept at 37.00°C . When the driving voltage from the function generator was increased from 54 to 59 mV, the ultrasound power was raised from 0.36 to 0.43 W. Thus, the heating speed was linearly increased from 14.87 to 17.06°C/s because it is positively related to the ultrasound intensity. Therefore, we expect that both t_a and t_b

will be shortened due to the heating speed increase. This is validated by the result in Fig. 5(a) in which t_a is shortened 0.10 s and t_b 0.15 s, respectively. A similar experiment was repeated when the background temperature was increased from 37.00 to 38.38 °C, and the results were displayed in Fig. 5(b) where t_a is shortened 0.03 s and t_b 0.02 s, respectively. These results in Fig. 5 indicate that the effect of the heating speed (i.e. ultrasound intensity) on t_a and t_b is more significant at lower background temperatures (relative to the T_a or T_b). This is understandable via one extreme example below. Imagining the background temperature is equal to T_a , ideally one can always have $t_a = 0$ s no matter how fast the heating speed is. Thus, increasing the heating speed will not be able to shorten t_a . However, this assumption does not hold when the background temperature is lower than T_a as seen in Fig. 5(a-b).

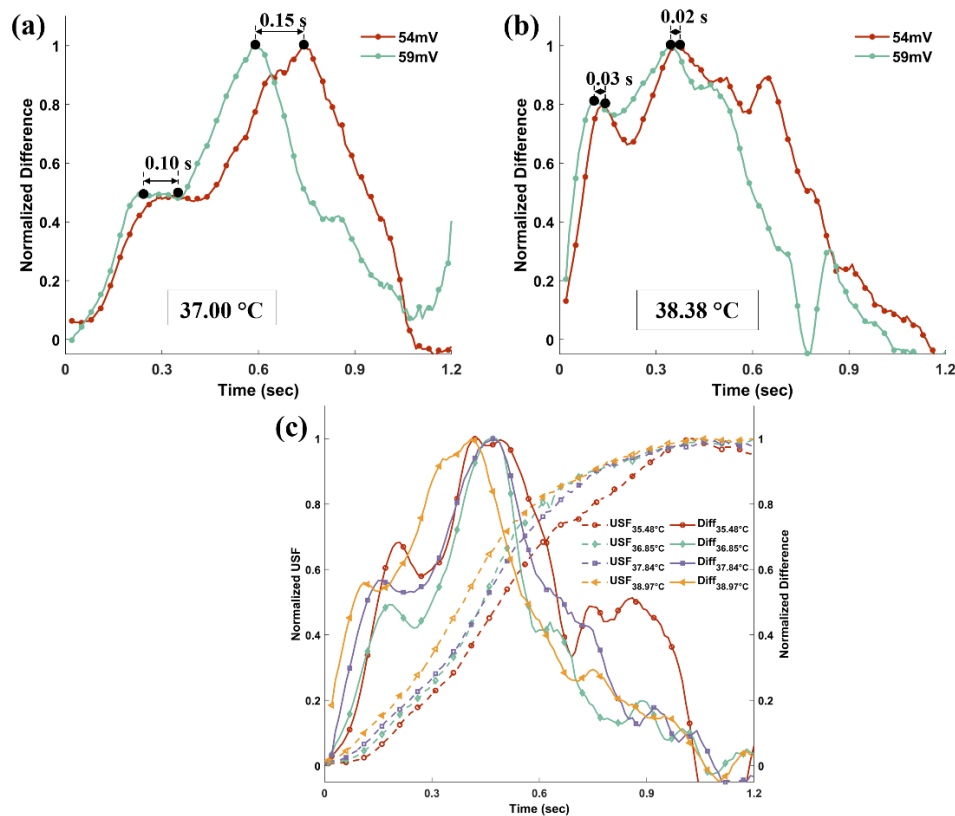


Fig. 5. (a) The temporal profiles of normalized differences of USF signal when switching the thermosensitive USF agents by different ultrasound parameters (54 vs. 59 mV). The background temperature is 37.00 °C. (b) Similar results obtained when background temperature is 38.38 °C. (c) The normalized USF signals and signal differences with time at selected background temperatures (35.48, 36.85, 37.84, and 38.97 °C). Diff: the differences of two adjacent points in the corresponding dashed line.

The dynamic USF signals and their differential curves acquired at different background temperature values (35.48, 36.85, 37.84, and 38.97 °C) are also plotted in Fig. 5(c). The USF signals are represented using dashed lines, while their differential results are presented using solid lines. When the background temperature is consistent, these signals are depicted using the same color and marker. The differential USF curves indicate that the switching peaks occur earlier as the background temperature increases, owing to the relatively constant heating speed, which leads to faster attainment of T_a and T_b . This is also the reason why the corresponding

USF signals display higher slopes, particularly at the start of the FU heating. The U.S. Food and Drug Administration (FDA) guidelines emphasize the importance of well-defined thermal effects and minimal side effects on surrounding tissues induced by FU. According to the thermal dose formulation, a thermal lesion along with thermal necrosis and the denaturing of tissue protein can form in 10 s at 53 °C [50]. Our experiments demonstrated that exposing tissue to ultrasound for 1.2 seconds raises the temperature from 36.80 to 52.98 °C, indicating a relatively low thermal damage. The mechanical index of FU used for USF thermometry is approximately 1.45, below the FDA limit for diagnostic ultrasound application at 1.9 [51]. Nevertheless, the exposure time can be further reduced to minimize thermal damage and allow for higher ultrasonic power on the condition that the second switching temperature (T_b) can be achieved. Additionally, future *ex/in vivo* studies using biological tissue which has a lower absorption coefficient than silicone tube in this feasibility study may allow higher ultrasonic voltage to be applied [38].

3.5. Limitations and advantages

The destabilization of the liposome membrane can occur due to hydrolysis and oxidation of lipids, resulting in the formation of soluble derivatives. Physical interactions such as aggregation and coalescence of liposomes can also lead to the loss of encapsulated molecules and changes in size. 30% of cholesterol is considered to be the most stable formulation according to the literature [52], but only approximately 10% molar ratio of cholesterol was added as stabilizer in the current protocol. This is because the transition bands of ICG-liposomes become wider as more cholesterol was added, which can negatively affect the sensitivity of agents at the switching temperature. Therefore, there are still concerns regarding the stability of ICG-liposomes at body temperature, which compromises the effective use of liposomes in the USF-based thermometry. It is also not clear if the instability of USF agents will shift the transition temperature, which may undermine the consistency and repeatability of the experiment data, and lead to fluctuations in temperature measurements.

The temperature estimation is only based on the information collected from two switching peaks, and therefore more switching temperature points possibly allow for higher accuracy and a broader estimation range. However, it will increase the complexity if more switching peaks are incorporated by adding extra varieties of ICG-liposomes with different threshold temperatures.

In addition, the linear heating assumption and the linear equation to calculate the heating speed may be replaced by more sophisticated models, such as thermal diffusion and photon diffusion to improve the accuracy.

While the background temperature estimation has only been demonstrated at a single point, the capability of USF thermometry to map two-dimensional temperature distribution by scanning is a non-negligible advantage. Imaging temperature at depths can be another potential of USF thermometry. A sub-millimeter tube in a 5.5 cm thick chicken breast tissue was successfully imaged using the same USF imaging system and similar ICG-liposomes agents, proving that the spatial imaging resolution remains relatively consistent at varying depths [44]. Therefore, the combination of temperature measurements and USF imaging at deep tissues in the same experiment holds another great potential. However, it is crucial to carefully select the appropriate exposure time and FU intensity for different samples and imaging depths to achieve accurate and reliable results. Further efforts to maintain an acceptable signal-to-noise ratio in the future *ex/in vivo* studies of this USF-based thermometry at a deeper level will be investigated.

4. Conclusion

In this study, we have demonstrated that the local background temperature can be estimated by analyzing the temperature-dependent fluorescence variations from USF contrast agents during ultrasound heating. The ICG-liposome agents provide a tunable measurement range that can be adjusted by modifying the compositions of the outer lipid shells. We tested this USF-thermometry

with the mixture of ICG-liposomes with two distinct temperature switching-on thresholds and recorded the dynamic USF signals using a camera-based USF system. By fitting the results into our customized algorithm, we can calculate the local background temperature of the sample over a typical physiological range. Our findings indicate that this USF technique-based temperature measurement provides accurate temperature readings, validated by an independent measurement from IR thermography, with a difference of only 0.64 ± 0.43 °C between the two techniques over a range of 35.27 to 39.31 °C.

The significant implications of this research lie in the potential for the USF-based thermometry technique to be applied to deep tissue temperature imaging applications. This approach provides an alternative method to current techniques, which are limited by the low sensitivity and inability to measure temperatures at depth. Further research can optimize USF contrast agents and advance the USF-based thermometry technique to enable its translation into in vivo and clinical settings. In summary, our study highlights the potential of USF-based thermometry as a valuable tool for future research and clinical practice, and this new temperature imaging method with a tunable measurement range makes it a great approach for a wide range of applications.

Funding. National Institute of Biomedical Imaging and Bioengineering (1R15EB030809-01).

Disclosures. B. Yuan has a potential research conflict of interest due to a financial interest with RCLabX LLC, which, however, did not support this work. A management plan has been created to preserve objectivity in research in accordance with UTA policy. Others declare no competing interests.

Data availability. Data underlying the results presented in this paper are available upon reasonable request.

Supplemental document. See [Supplement 1](#) for supporting content.

References

1. J. P. Knapp, J. E. Kakish, B. W. Bridle, and D. J. Speicher, "Tumor temperature: friend or foe of virus-based cancer immunotherapy," *Biomedicines* **10**(8), 2024 (2022).
2. C. Stefanadis, C. Chrysohoou, D. B. Panagiotakos, E. Passalidou, V. Katsi, V. Polychronopoulos, and P. K. Toutouzas, "Temperature differences are associated with malignancy on lung lesions: a clinical study," *BMC Cancer* **3**(1), 1 (2003).
3. C. Stefanadis, C. Chrysohoou, D. Markou, K. Petraki, D. B. Panagiotakos, C. Fasoulakis, A. Kyriakidis, C. Papadimitriou, and P. K. Toutouzas, "Increased temperature of malignant urinary bladder tumors in vivo: the application of a new method based on a catheter technique," *J. Clin. Oncol.* **19**(3), 676–681 (2001).
4. T. Yahara, T. Koga, S. Yoshida, S. Nakagawa, H. Deguchi, and K. Shirouzu, "Relationship between microvessel density and thermographic hot areas in breast cancer," *Surg. Today* **33**(4), 243–248 (2003).
5. Q. Zhao, J. Zhang, R. Wang, and W. Cong, "Use of a thermocouple for malignant tumor detection," *IEEE Eng. Med. Biol. Mag.* **27**(1), 64–66 (2008).
6. M. Gautherie, "Thermopathology of breast cancer: measurement and analysis of in vivo temperature and blood flow," *Ann. N. Y. Acad. Sci.* **335**(1 Thermal Chara), 383–415 (1980).
7. M. Gautherie, "Thermobiological assessment of benign and malignant breast diseases," *Am. J. Obstet. Gynecol.* **147**(8), 861–869 (1983).
8. S. A. Feig, G. S. Shaber, G. F. Schwartz, A. Patchefsky, H. I. Libshitz, J. Edeiken, R. Nerlinger, R. F. Curley, and J. D. Wallace, "Thermography, mammography, and clinical examination in breast cancer screening: review of 16,000 studies," *Radiology* **122**(1), 123–127 (1977).
9. R. N. Lawson and M. S. Chughtai, "Breast cancer and body temperature," *Can. Med. Assoc. J.* **88**(2), 68–70 (1963).
10. J. D. Wallace and G. D. Dodd, "Thermography in the diagnosis of breast cancer," *Radiology* **91**(4), 679–685 (1968).
11. M. Moskowitz, J. Milbrath, P. Gartside, A. Zermeno, and D. Mandel, "Lack of efficacy of thermography as a screening tool for minimal and stage i breast cancer," *N. Engl. J. Med.* **295**(5), 249–252 (1976).
12. G. C. Wishart, M. Campisi, M. Boswell, D. Chapman, V. Shackleton, S. Iddles, A. Hallett, and P. D. Britton, "The accuracy of digital infrared imaging for breast cancer detection in women undergoing breast biopsy," *Eur. J. Surg. Oncol. EJSO* **36**(6), 535–540 (2010).
13. N. Arora, D. Martins, D. Ruggerio, E. Tousimis, A. J. Swistel, M. P. Osborne, and R. M. Simmons, "Effectiveness of a noninvasive digital infrared thermal imaging system in the detection of breast cancer," *Am. J. Surg.* **196**(4), 523–526 (2008).
14. N. F. Boyd, L. J. Martin, M. Bronskill, M. J. Yaffe, N. Duric, and S. Minkin, "Breast tissue composition and susceptibility to breast cancer," *J. Natl. Cancer Inst.* **102**(16), 1224–1237 (2010).
15. P. C. Gøtzsche and K. J. Jørgensen, "Screening for breast cancer with mammography," *Cochrane Database Syst. Rev.* **2013**(6), CD001877 (2013).

16. S. H. Heywang-Köbrunner, A. Hacker, and S. Sedlacek, "Advantages and disadvantages of mammography screening," *Breast Care* **6**(3), 2 (2011).
17. V. Rieke and K. Butts Pauly, "MR thermometry," *J. Magn. Reson. Imaging* **27**(2), 376–390 (2008).
18. J. Yuan, C. S. Mei, L. P. Panych, N. J. McDannold, and B. Madore, "Towards fast and accurate temperature mapping with proton resonance frequency-based MR thermometry," *Quant. Imaging Med. Surg.* **2**(1), 21 (2012).
19. L. H. Lindner, H. M. Reinl, M. Schlemmer, R. Stahl, and M. Peller, "Paramagnetic thermosensitive liposomes for MR-thermometry," *Int. J. Hyperthermia* **21**(6), 575–588 (2005).
20. M. A. Lewis, R. M. Staruch, and R. Chopra, "Thermometry and ablation monitoring with ultrasound," *Int. J. Hyperthermia* **31**(2), 163–181 (2015).
21. J. Yao, H. Ke, S. Tai, Y. Zhou, and L. V. Wang, "Absolute photoacoustic thermometry in deep tissue," *Opt. Lett.* **38**(24), 5228–5231 (2013).
22. R. O. Esenaliev, A. A. Oraevsky, K. V. Larin, I. V. Larina, and M. Motamedi, "Real-time optoacoustic monitoring of temperature in tissues," *Proc. SPIE* **3601**, 268–275 (1999).
23. K. V. Larin, I. V. Larina, M. Motamedi, and R. O. Esenaliev, "Monitoring of temperature distribution in tissues with optoacoustic technique in real time," *Proc. SPIE* **3916**, 311–321 (2000).
24. I. V. Larina, K. V. Larin, and R. O. Esenaliev, "Real-time optoacoustic monitoring of temperature in tissues," *J. Phys. D: Appl. Phys.* **38**(15), 2633–2639 (2005).
25. A. Hariri, J. Lemaster, J. Wang, A. S. Jeevarathinam, D. L. Chao, and J. V. Jokerst, "The characterization of an economic and portable LED-based photoacoustic imaging system to facilitate molecular imaging," *Photoacoustics* **9**, 10–20 (2018).
26. M. W. Schellenberg and H. K. Hunt, "Hand-held optoacoustic imaging: a review," *Photoacoustics* **11**, 14–27 (2018).
27. H. Zhong, T. Duan, H. Lan, M. Zhou, and F. Gao, "Review of low-cost photoacoustic sensing and imaging based on laser diode and light-emitting diode," *Sensors* **18**(7), 2264 (2018).
28. Y. Zhou, E. Tang, J. Luo, and J. Yao, "Deep-tissue temperature mapping by multi-illumination photoacoustic tomography aided by a diffusion optical model: a numerical study," *J. Biomed. Opt.* **23**(12), 1 (2018).
29. L. Meng, O. Deschaume, L. Larbanoix, E. Fron, C. Bartic, S. Laurent, M. Van Der Auweraer, and C. Glorieux, "Photoacoustic temperature imaging based on multi-wavelength excitation," *Photoacoustics* **13**, 33–45 (2019).
30. M. A. O'Leary, D. A. Boas, B. Chance, and A. G. Yodh, "Experimental images of heterogeneous turbid media by frequency-domain diffusing-photon tomography," *Opt. Lett.* **20**(5), 426 (1995).
31. R. M. Verdaasdonk, C. F. P. Van Swol, M. C. M. Grimbergen, and A. I. Rem, "Imaging techniques for research and education of thermal and mechanical interactions of lasers with biological and model tissues," *J. Biomed. Opt.* **11**(4), 041110 (2006).
32. J. Shah, S. Park, S. Aglyamov, T. Larson, L. Ma, K. Sokolov, K. Johnston, T. Milner, and S. Y. Emelianov, "Photoacoustic imaging and temperature measurement for photothermal cancer therapy," *J. Biomed. Opt.* **13**(3), 034024 (2008).
33. M. Pramanik and L. V. Wang, "Thermoacoustic and photoacoustic sensing of temperature," *J. Biomed. Opt.* **14**(5), 054024 (2009).
34. Y. H. Liu, Y. Xu, L. D. Liao, K. Chan, and N. Thakor, "A handheld real-time photoacoustic imaging system for animal neurological disease models: from simulation to realization," *Sensors* **18**(11), 4081 (2018).
35. Y. Zhou, M. Li, W. Liu, G. Sankin, J. Luo, P. Zhong, and J. Yao, "Thermal memory based photoacoustic imaging of temperature," *Optica* **6**(2), 198 (2019).
36. L. Ren, Y. Liu, T. Yao, K. T. Nguyen, and B. Yuan, "In vivo tumor ultrasound-switchable fluorescence imaging via intravenous injections of size-controlled thermosensitive nanoparticles," *Nano Res.* **9**(1), 9855 (2019).
37. Y. Pei, M. Y. Wei, B. Cheng, Y. Liu, Z. Xie, K. Nguyen, and B. Yuan, "High resolution imaging beyond the acoustic diffraction limit in deep tissue via ultrasound-switchable NIR fluorescence," *Sci. Rep.* **4**(1), 4690 (2014).
38. T. Yao, S. Yu, Y. Liu, and B. Yuan, "In vivo ultrasound-switchable fluorescence imaging," *Sci. Rep.* **9**(1), 9855 (2019).
39. B. Yuan, S. Uchiyama, Y. Liu, K. T. Nguyen, and G. Alexandrakis, "High-resolution imaging in a deep turbid medium based on an ultrasound-switchable fluorescence technique," *Appl. Phys. Lett.* **101**(3), 033703 (2012).
40. B. Cheng, V. Bandi, M. Y. Wei, Y. Pei, F. D'Souza, K. T. Nguyen, Y. Hong, and B. Yuan, "High-resolution ultrasound-switchable fluorescence imaging in centimeter-deep tissue phantoms with high signal-to-noise ratio and high sensitivity via novel contrast agents," *PLoS ONE* **11**(11), e0165963 (2016).
41. Y. Liu, T. Yao, W. Cai, S. Yu, Y. Hong, K. T. Nguyen, and B. Yuan, "A Biocompatible and Near-Infrared Liposome for In Vivo Ultrasound-Switchable Fluorescence Imaging," *Adv. Healthcare Mater.* **9**(4), 1901457 (2020).
42. Y. Liu, T. Yao, L. Ren, and B. Yuan, "Size effect of liposomes on centimeter-deep ultrasound-switchable fluorescence imaging and ultrasound-controlled release," *J. Mater. Chem. B* **10**(43), 8970–8980 (2022).
43. M. Pons, M. Foradada, and J. Estelrich, "Liposomes obtained by the ethanol injection method," *Int. J. Pharm.* **95**(1–3), 51–56 (1993).
44. T. Yao, Y. Liu, L. Ren, and B. Yuan, "Improving sensitivity and imaging depth of ultrasound-switchable fluorescence via an EMCCD-gain-controlled system and a liposome-based contrast agent," *Quant. Imaging Med. Surg.* **11**(3), 957–968 (2020).
45. T. Yao, S. Yu, Y. Liu, and B. Yuan, "Ultrasound-switchable fluorescence imaging via an EMCCD camera and a Z-scan method," *IEEE J. Sel. Top. Quantum Electron.* **25**(2), 1–8 (2019).

46. R. Liu, T. Yao, Y. Liu, S. Yu, L. Ren, Y. Hong, K. T. Nguyen, and B. Yuan, "Temperature-sensitive polymeric nanogels encapsulating with β -cyclodextrin and ICG complex for high-resolution deep-tissue ultrasound-switchable fluorescence imaging," *Nano Res.* **13**(4), 1100–1110 (2020).
47. T. Lu and T. L. M. ten Hagen, "Inhomogeneous crystal grain formation in DPPC-DSPC based thermosensitive liposomes determines content release kinetics," *J. Controlled Release* **247**, 64–72 (2017).
48. B. Yuan, Y. Pei, and J. Kandukuri, "Breaking the acoustic diffraction limit via nonlinear effect and thermal confinement for potential deep-tissue high-resolution imaging," *Appl. Phys. Lett.* **102**(6), 063703 (2013).
49. M. Anderson and A. Omri, "The effect of different lipid components on the in vitro stability and release kinetics of liposome formulations," *Drug Delivery* **11**(1), 33–39 (2004).
50. T. D. Khokhlova and J. H. Hwang, "HIFU for palliative treatment of pancreatic cancer," *J. Gastrointest. Oncol.* **2**(3), 83–95 (2011).
51. S. B. Barnett, G. R. Ter Haar, M. C. Ziskin, H.-D. Rott, F. A. Duck, and K. Maeda, "International recommendations and guidelines for the safe use of diagnostic ultrasound in medicine," *Ultrasound Med. Biol.* **26**(3), 355–366 (2000).
52. M. L. Bruggia, C. Rotella, A. McFarlane, and D. A. Lamprou, "Influence of cholesterol on liposome stability and on in vitro drug release," *Drug Deliv. Transl. Res.* **5**(3), 231–242 (2015).